Optimal Switching Sequence MPC of a Three-Port-Converter for Variable-Speed PMSM With Hybrid Energy Storage

Felipe Rubio, Javier Pereda, *Senior Member, IEEE*, Andrés Mora, *Member, IEEE*, and Félix Rojas, *Member, IEEE*

***Abstract*—This article presents a model predictive current control strategy utilizing optimal switching sequences for two-level, three-port converters driving an anisotropic permanent magnet synchronous machine (PMSM). These converters are attractive in hybrid energy systems, including fuel cell electric vehicles and hybrid energy storage systems. The proposed control method optimally calculates the switching vectors and duty cycles for both steady-state and transient conditions, including during overmodulation, a scenario that introduces significant optimization challenges. The strategy proposes a simple second stage of control to govern the dc port current, exploiting the redundancy of passive vectors, and eliminating the need for weighting factors to balance the control objectives between the PMSM and the energy storage system, giving absolute priority to the control of the PMSM. Experimental results on a laboratory-scale prototype demonstrate the controller high-dynamic performance in regulating torque, speed, and power transfer across multiple ports, while also maintaining a fixed switching frequency and a well-defined harmonic spectrum.**

***Index Terms*—Hybrid energy storage systems (HESSs), model predictive control (MPC), multiport converters, optimal switching sequence (OSS), permanent magnet synchronous machine (PMSM).**

NOMENCLATURE

$\boldsymbol{u}_{\text{abc}}$	abc switching vector.
$\boldsymbol{v}_{\text{abc}N}$	abc voltage vector.
$\boldsymbol{u}_{\alpha\beta}$	$\alpha\beta$ switching vector.
$\boldsymbol{v}_{\alpha\beta}$	$\alpha\beta$ voltage vector.
$\boldsymbol{u}_{\text{s}}$	Average switching vector in $\alpha\beta$ coordinates.
$\boldsymbol{v}_{\text{s}}$	Average voltage vector in $\alpha\beta$ coordinates.
$\boldsymbol{i}_{\text{s}}$	Stator current vector in $\alpha\beta$ coordinates.
$\boldsymbol{v}_{\text{ind}}$	Machine back-EMF.
θ_r	Electric rotor position.
$\boldsymbol{d}$	Duty cycle vector.
$\boldsymbol{U}$	Switching matrix.
ϑ	Distribution parameter of passive vectors.
u_0	Common mode of a signal $\boldsymbol{u}$.
$\boldsymbol{u}_0$	Common mode vector of the switching sequence.
U_0	Average common mode of the switching sequence.

Received 9 July 2024; revised 19 October 2024; accepted 6 December 2024. Date of publication 23 December 2024; date of current version 28 January 2025. This work was supported in part by ANID (National Agency for Research and Development, Chile) under Fondecyt under Grant 1220928, Grant 1231030, and Grant Fondap 1523A0006 (SERC-Chile), and in part by Basal Project AFB240002 (AC3E). An earlier version of this paper was presented in part at the 2023 IEEE Energy Conversion Congress and Exposition (ECCE) [DOI: 10.1109/ECCE53617.2023.10362681]. Recommended for publication by Associate Editor K. Ma. *(Corresponding author: Javier Pereda.)*

Felipe Rubio, Javier Pereda, and Félix Rojas are with the Department of Electrical Engineering and the UC Energy Research Center, Pontificia Universidad Católica de Chile, Santiago 7820436, Chile (e-mail: fnrubio@uc.cl; jepereda@uc.cl; felix.rojas@uc.cl).

Andrés Mora is with the Department of Electrical Engineering, Universidad Tecnica Federico Santa Maria, Valparaiso 2390123, Chile (e-mail: andres.mora@usm.cl).

Color versions of one or more figures in this article are available at https://doi.org/10.1109/TPEL.2024.3521504.

Digital Object Identifier 10.1109/TPEL.2024.3521504

I. INTRODUCTION

THE integration of renewable energy resources and energy storage systems is crucial in modern power generation and usage, especially in industries and transportation where electric machines are predominant [2]. Multiport converters play a vital role in providing efficient, low-cost, and streamlined solutions for integrating these technologies [3]. The two-level three-port converter topology (2L-TPC) has emerged as a promising option compared to classical two-level converters cascaded with buck–boost converters to achieve fast dynamic response, proper coupling between the two stages and high efficiency [4]. Controlling the output current of this converter is a critical aspect in applications using drives, especially in machines that require high dynamic response and in applications that require high precision in the dc outputs [1]. Consequently, some of the desired characteristics of current control are: 1) accuracy; 2) high bandwidth; 3) fast dynamic response; and 4) low harmonic distortion [5].

The development of more powerful microprocessors has motivated the exploration of more sophisticated strategies to control power converters. In this scenario, model predictive control (MPC) has established itself as a promising control methodology [6]. In the context of power electronics and electric drives, MPC methods are classified depending on how the switching devices are controlled and, consequently, on the type of optimization problem posed to compute the optimal control actions [7]. MPC methods can be classified into two broad categories as follows. 1) Indirect MPC, where the controller calculates a continuous control signal, and then uses a modulator to generate the desired voltage. 2) Direct MPC (DMPC), where

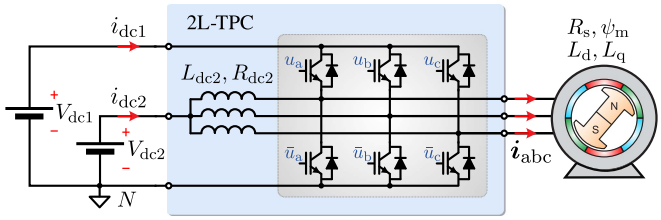

Fig. 1. 2L-TPC topology driving a PMSM.

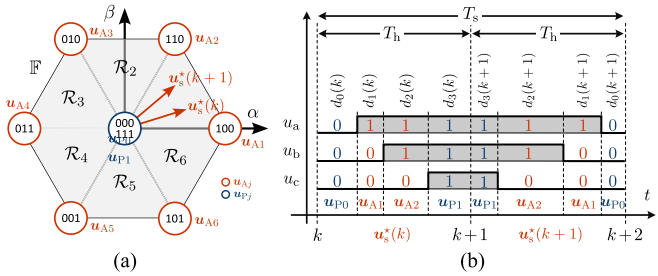

Fig. 2. SV selection for OSS current control. (a) SVs region. (b) 7S-SS for $\mathcal{R}_1$ region.

the controller performs in a single computational stage the calculation of the control action to be applied, without requiring an external modulator [8]. Among the DMPC schemes, the finite control set (FCS-MPC) sometimes called optimal switching vector (OSV-MPC) is one of the most popular for its intuitive design, easy implementation and fast response [9]. FCS-MPC directly uses the possible switching vectors to define the feasible control set. In this way, the algorithm searches for the switching action that minimizes a cost function by quantifying the tracking error and the switching effort. This approach has been introduced in [10] for 2L-TPC converter control and is well studied for machine control on typical 2L converters [11]. However, these methods require weighting factors to compensate for switching effort and tracking error, and produce a variable switching frequency in the output voltages, and higher ripple in the current shapes than techniques that include modulation stages at similar switching frequencies [12].

Motivated by the aforementioned concerns, this article presents a predictive current control strategy based on optimal switching sequences (OSSs) for two-level, three-port converters (2L-TPC) driving anisotropic PMSMs. While the 2L-TPC topology itself is not new, the novelty of this work lies in the proposed control and inclusion of the anisotropic PMSM.

The first innovation is in the PMSM control algorithm, which determines the optimal region and application times for the switching vectors, enabling optimal sequences under both stationary and transient conditions—even during overmodulation. This is particularly challenging for anisotropic PMSMs, but the proposed method achieves reduced harmonic distortion, a fixed switching frequency, and fast dynamic response without compromising the benefits of MPC strategies.

The second novelty utilizes the redundancy of passive vectors to regulate the current on one of the TPC dc ports. This approach is both simpler and more effective, as it prioritizes PMSM control while eliminating the need for weighting factors in the objective function. This allows for seamless simultaneous operation of the PMSM and energy storage system.

Experimental results are provided with a 2L-TPC prototype feeding a PMSM of 11 kW to verify the proposal's performance and effectiveness under steady state, transients, and different operation modes.

II. Model of the 2L-TPC

The schematic of a 2L-TPC connected to a PMSM at its ac port and to two voltage sources at its dc ports is shown in Fig. 1. The converter is simple and comprises two switches in each leg, producing a total of 2^3 switching positions $\boldsymbol{u}_{\text{abc}} \in \mathbb{U} \triangleq \{0,1\}^3$. The ac output of each phase can take a value of 0 or V_{dc1} V respect to the neutral of the N converter, and the voltage on each parasitic inductor can have a value of $V_{\text{dc1}} - V_{\text{dc2}}$ or $-V_{\text{dc2}}$ V. The three-phase output voltage vector can be defined as a function of these positions as follows:

$$\boldsymbol{v}_{\text{abc}N} = V_{\text{dc1}}\boldsymbol{u}_{\text{abc}} = V_{\text{dc1}}\begin{bmatrix} u_{\text{a}} & u_{\text{b}} & u_{\text{c}} \end{bmatrix}^\top \tag{1}$$

where $\boldsymbol{u}_{\text{abc}}$ is the three-phase switching state of the converter. Using the amplitude-invariant Clarke transform $\mathbf{T}_{\alpha\beta}$ [13], it is possible to represent $\boldsymbol{u}_{\text{abc}}$ in the $\alpha\beta$ frame as follows:

$$\boldsymbol{u}_{\alpha\beta} = \begin{bmatrix} u_\alpha & u_\beta \end{bmatrix}^\top = \mathbf{T}_{\alpha\beta}\boldsymbol{u}_{\text{abc}} \in \mathcal{U} \triangleq \mathbf{T}_{\alpha\beta}\mathbb{U}. \tag{2}$$

Thus, the voltage vector in $\alpha\beta$ coordinates is $\boldsymbol{v}_{\alpha\beta} = V_{\text{dc1}}\boldsymbol{u}_{\alpha\beta}$, where six active (nonredundant) vectors $\{\boldsymbol{u}_{\text{A1}}, \ldots, \boldsymbol{u}_{\text{A6}}\} \triangleq \mathcal{A}$ and two passive (redundant) vectors $\{\boldsymbol{u}_{\text{P0}}, \boldsymbol{u}_{\text{P1}}\} \triangleq \mathcal{P}$ can be distinguished. To synthesize a desired average switching vector (ASV) $\boldsymbol{u}_{\text{s}}$, it is proposed to use an asymmetric 7S-SS due to the low inductance of the machine. Thus, for every switching cycle, the proposed controller samples twice for every switching cycle, working in a double-update fashion. Therefore, during each half-switching period $T_{\text{h}} = T_{\text{s}}/2$, a target vector can be formed by a switching sequence (SS) $\boldsymbol{S}^\star$ made up of both redundancies of the passive vector and two adjacent active vectors $\{\boldsymbol{u}_1, \boldsymbol{u}_2\} \subset \mathcal{A}$ associated with the region where $\boldsymbol{u}_{\text{s}}^\star$ is located. Fig. 2(a) shows that the feasible space for the space vectors (SVs) $\mathbb{F}$ is divided into six regions $\mathcal{R}_j \in \mathcal{R} \triangleq \{\mathcal{R}_1, \ldots, \mathcal{R}_6\}$. In the case of Fig. 2, both objective vectors $\boldsymbol{u}_{\text{s}}^\star(k)$ and $\boldsymbol{u}_{\text{s}}^\star(k+1)$ belong to $\mathcal{R}_1$, therefore $\boldsymbol{u}_1 = \boldsymbol{u}_{\text{A1}}$ and $\boldsymbol{u}_2 = \boldsymbol{u}_{\text{A2}}$. Each vector is applied for a time t_i so that $d_i = t_i/T_{\text{h}} \in \mathbb{D} \triangleq [0,1]$ corresponds to the duty cycle of the ith switching vector $\boldsymbol{u}_i$ considering $\boldsymbol{u}_0 = \boldsymbol{u}_{\text{p0}}$ and $\boldsymbol{u}_3 = \boldsymbol{u}_{\text{p1}}$. Therefore, for any SS, it is possible to generate any ASV $\boldsymbol{u}_{\text{s}} \in \mathbb{F}$ during a switching half-period T_{h}.

A. Discrete-Time Model for Machine Current Control

To formulate the control strategy, the continuous-time model of the PMSM shown in Fig. 1 is expressed in $\alpha\beta$ coordinates as [14], [15] follows:

$$\frac{\text{d}\boldsymbol{i}_{\text{s}}}{\text{d}t} = \mathbf{F}\boldsymbol{i}_{\text{s}} + \mathbf{G}\boldsymbol{v}_{\text{ind}} + \mathbf{H}\boldsymbol{u}_{\text{s}} \tag{3}$$

where $\boldsymbol{i}_{\text{s}} = \begin{bmatrix} i_{s\alpha} & i_{s\beta} \end{bmatrix}^\top = \mathbf{T}_{\alpha\beta}\boldsymbol{i}_{\text{abc}}$ is the stator current vector, $\boldsymbol{v}_{\text{ind}} = \psi_{\text{m}}\omega_{\text{r}}\begin{bmatrix} -\sin(\theta_{\text{r}}) & \cos(\theta_{\text{r}}) \end{bmatrix}^\top$ is the machine back-EMF, which is produced by the stator flux linkage due to the rotor

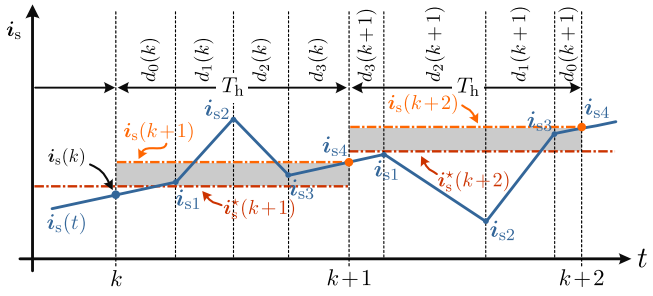

Fig. 3. Predicted system trajectory for an asymmetric 7S-SS.

magnets, and $\mathbf{F}$, $\mathbf{G}$, and $\mathbf{H}$ are matrices depending on the rotor position θ_r given by $\mathbf{F} = -\mathbf{L}_{\alpha\beta}^{-1}(\mathbf{R}+\mathbf{W})$, $\mathbf{G} = -\mathbf{L}_{\alpha\beta}^{-1}$, and $\mathbf{H} = V_{\rm dc1}\mathbf{L}_{\alpha\beta}^{-1}$, with

$$\mathbf{L}_{\alpha\beta} = \begin{bmatrix} L_1 + L_2\cos(2\theta_{\rm r}) & L_2\sin(2\theta_{\rm r}) \\ L_2\sin(2\theta_{\rm r}) & L_1 - L_2\cos(2\theta_{\rm r}) \end{bmatrix} \tag{4}$$

$$\mathbf{W} = \omega_{\rm r}\frac{\partial \mathbf{L}_{\alpha\beta}}{\partial\theta_{\rm r}} = 2\omega_{\rm r}L_2\begin{bmatrix} -\sin(2\theta_{\rm r}) & \cos(2\theta_{\rm r}) \\ \cos(2\theta_{\rm r}) & \sin(2\theta_{\rm r}) \end{bmatrix} \tag{5}$$

$$\mathbf{R} = \mathrm{diag}\{R_{\rm s},\, R_{\rm s},\, R_{\rm s}\} \tag{6}$$

where $L_1 = \frac{L_{\rm d}+L_{\rm q}}{2}$ and $L_2 = \frac{L_{\rm d}-L_{\rm q}}{2}$, being $L_{\rm d}$ and $L_{\rm q}$ the direct and quadrature axis inductance, respectively, and $R_{\rm s}$ the stator winding resistance.

To model the trajectory of the stator current toward the end of a switching half-period $T_{\rm h}$, two assumptions are made. First, the interval $T_{\rm h}$ is much smaller than the shortest time constant of the system, i.e., $T_{\rm h} \ll \frac{1}{2}(L_{\rm d}+L_{\rm q})/R_{\rm s}$. Consequently, when the converter applies a given 7S-SS, the stator current $\boldsymbol{i}_{\rm s}(t)$ evolves linearly over each subinterval t_i. Therefore, the trajectory can be considered as a piecewise linear function of time, as illustrated in Fig. 3. Thus, the predicted trajectory of $\boldsymbol{i}_{\rm s}$ can be computed sequentially using the forward Euler method as follows:

$$\boldsymbol{i}_{{\rm s}(i+1)} = \boldsymbol{i}_{{\rm s}(i)} + \left.\frac{{\rm d}\boldsymbol{i}_{\rm s}}{{\rm d}t}\right|_i T_{\rm h} d_i. \tag{7}$$

Therefore, when the converter applies the 7S-SS, the stator current at the end of the subcycle is given by

$$\boldsymbol{i}_{\rm s}(k+1) = \boldsymbol{i}_{\rm s}(k) + T_{\rm h}\sum_{i=0}^{3}\left.\frac{{\rm d}\boldsymbol{i}_{\rm s}}{{\rm d}t}\right|_i d_i. \tag{8}$$

Second, the fundamental period of the stator voltages is assumed to be much larger than $T_{\rm h}$. Then, every subinterval gradient, i.e., $\frac{{\rm d}\boldsymbol{i}_{\rm s}}{{\rm d}t}|_i$, is calculated using the sampled values of the system's variables. Consequently, introducing the duty cycle vector $\boldsymbol{d}(k)$ and the switching matrix $\boldsymbol{U}(k)$ defined as follows:

$$\boldsymbol{d}(k) \triangleq \begin{bmatrix} d_{\rm p}(k) & d_1(k) & d_2(k) \end{bmatrix}^\top \in \mathbb{D} \triangleq [0,1]^3 \tag{9}$$

$$\boldsymbol{U}(k) \triangleq \begin{bmatrix} \boldsymbol{u}_{\rm p}(k) & \boldsymbol{u}_1(k) & \boldsymbol{u}_2(k) \end{bmatrix} \in \mathcal{M}_{2\times 3}(\mathbb{R}) \tag{10}$$

with $d_{\rm p} = d_0 + d_3$, the ASV can be expressed by $\boldsymbol{u}_{\rm s}(k) = \boldsymbol{U}(k)\boldsymbol{d}(k)$ and consequently, the prediction of the stator current in (8) can be expressed as follows:

$$\boldsymbol{i}_{\rm s}(k+1) = \mathbf{A}(k)\boldsymbol{i}_{\rm s}(k) + \mathbf{C}(k)\boldsymbol{v}_{\rm ind}(k) + \mathbf{B}(k)\boldsymbol{U}(k)\boldsymbol{d}(k) \tag{11}$$

where $\mathbf{A} = (T_{\rm h}\mathbf{F} + \mathbf{I}_2)$, $\mathbf{C} = T_{\rm h}\mathbf{G}$ y $\mathbf{B} = T_{\rm h}\mathbf{H}$.

B. Discrete-Time Model for Dc Current Control

To control the current in the second dc-link port ($i_{\rm dc2}$), this work uses the dwell-time distribution of the passive vectors. Thus, the duty cycle for the passive vector and its redundancy can be parameterized by using $\vartheta \in [0,\, 1]$ such that

$$d_0 = \vartheta d_{\rm p} \quad ; \quad d_3 = (1-\vartheta)d_{\rm p} \tag{12}$$

where $d_{\rm p}$ is the passive vector duty cycle to be distributed. This means that a value of $\vartheta = 0$ only uses the redundancy of the passive vector $\boldsymbol{u}_{\rm P0}$ while $\vartheta = 1$ only uses the redundancy of the passive vector $\boldsymbol{u}_{\rm p1}$. The duty cycle distribution presented in (12) only impacts the common-mode voltage applied by the converter. Thus, it does not affect the prediction of the stator current in (11), so it can be considered a degree of freedom to control $i_{\rm dc2}$. In this regard, the common-mode switching signal CMSS is defined as $u_0 = \frac{1}{3}(u_{\rm a}+u_{\rm b}+u_{\rm c})$. Therefore, the average CMSS can be expressed by

$$U_0(k) = \boldsymbol{u}_0^\top(k)\boldsymbol{d}(k) = d_1 u_{0(1)} + d_2 u_{0(2)} + \vartheta d_{\rm p} \tag{13}$$

where $u_{0(1)}$ and $u_{0(2)}$ correspond to the CMSS of the active switching vectors $\{\boldsymbol{u}_1, \boldsymbol{u}_2\}$, respectively. Accordingly, the dynamic equation governing the current $i_{\rm dc2}$ during a switching half-period $T_{\rm h}$ in terms of the average CMSS is [1]

$$\frac{{\rm d}i_{\rm dc2}}{{\rm d}t} = \frac{1}{L_{\rm dc2}}\Big[-R_{\rm dc2}i_{\rm dc2} + 3(V_{\rm dc2} - V_{\rm dc1})U_0(k)\Big] \tag{14}$$

which is simple, but relevant to determine the behavior of $i_{\rm dc2}$. Therefore, using the forward Euler method, when the converter applies the 7S-SS, the prediction of the current in the second dc-port is given by

$$i_{\rm dc2}(k+1) = \alpha_2 i_{\rm dc2}(k) + p_2(k) + \beta_2\vartheta(k) \tag{15}$$

where $\alpha_2 = 1 - T_{\rm h}\frac{R_{\rm dc2}}{L_{\rm dc2}}$, $\beta_2 = 3\frac{T_{\rm h}}{L_{\rm dc2}}(V_{\rm dc2} - V_{\rm dc1})d_{\rm p}$ is the input gain, and $p_2 = 3\frac{T_{\rm h}}{L_{\rm dc2}}(V_{\rm dc2} - V_{\rm dc1})(d_1 u_{0(1)} + d_2 u_{0(2)})$ is a known disturbance.

III. Speed and Current Control Method

The complete control scheme is illustrated in Fig. 4, where the series connection of the speed controller with the cascaded OSS-MPC can be seen.

A. Speed Controller

To formulate the control strategy, a speed linear controller determines the reference torque $T_{\rm e}^\star$. The reference torque can also be imposed directly. For simplicity, the d-axis current is regulated to zero, and the PMSM will only produce torque with the q-axis current. Thus, the current component references in the rotor reference frame are given by

$$i_{\rm d}^\star = 0 \quad ; \quad i_{\rm q}^\star = \frac{2T_{\rm e}^\star}{3p\psi_{\rm m}} \tag{16}$$

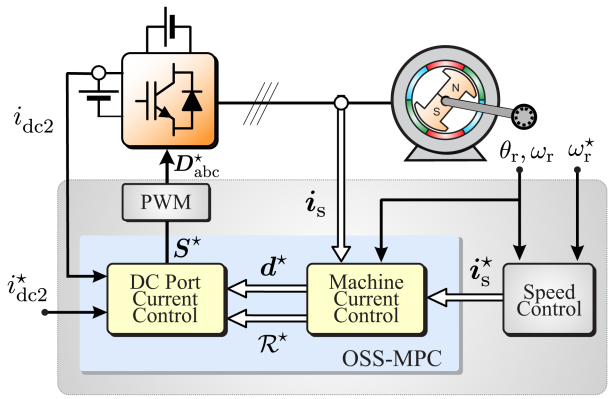

Fig. 4. Proposed OSS-MPC with external speed controller.

where p is the PMSM's pole pairs. Thus, by using the (reduced) inverse Park transform, the stator current reference in the $\alpha\beta$ reference frame can be expressed by

$$\boldsymbol{i}^{\star}_{s} = \mathbf{T}^{-1}_{dq}\left(\theta_r\right)\begin{bmatrix} i^{\star}_{d} & i^{\star}_{q}\end{bmatrix}^{\top}. \tag{17}$$

Fig. 4 illustrates how the speed controller sends the current references to the MPC-based machine current control, which is the first stage of the proposed OSS-MPC controller.

B. Machine Current Control

To obtain the optimal duty cycles for every SS candidate $\{\boldsymbol{U}^{\star}, \boldsymbol{d}^{\star}\}$, the following objective function is introduced:

$$J_j = \|\boldsymbol{i}_s(k+1) - \boldsymbol{i}^{\star}_s(k+1)\|^2_2 + \|\boldsymbol{\Lambda}_u\left(\boldsymbol{u}(k) - \boldsymbol{u}_{ss}(k)\right)\|^2_2. \tag{18}$$

This quadratic cost function is formulated to quantify two control objectives; the tracking error, and the control effort. The diagonal matrix $\boldsymbol{\Lambda}_u$ is used to adjust the compromise between both control objectives, avoiding the proposed OSS-MPC behaving like a deadbeat controller and producing robustness issues [7]. Then, by substituting (11) into (18), the cost function can be rewritten as

$$\begin{aligned} J_j = &\left\|\mathbf{B}\left(\boldsymbol{U}_j\boldsymbol{d}_j(k) - \boldsymbol{u}_{db}(k)\right)\right\|^2_2 \\ &+ \left\|\boldsymbol{\Lambda}_u\left(\boldsymbol{U}_j\boldsymbol{d}_j(k) - \boldsymbol{u}_{ss}(k)\right)\right\|^2_2 \end{aligned} \tag{19}$$

where $\boldsymbol{u}_{db}(k)$ is the deadbeat control input, and $\boldsymbol{u}_{ss}(k)$ is the steady-state control input, both defined as follows:

$$\boldsymbol{u}_{db}(k) = \mathbf{B}^{-1}\left(\boldsymbol{i}^{\star}_s(k+1) - \mathbf{A}\boldsymbol{i}_s(k) - \mathbf{C}\boldsymbol{v}_{ind}(k)\right) \tag{20}$$

$$\boldsymbol{u}_{ss}(k) = \frac{1}{V_{dc1}}\left[\left(\mathbf{R} + \mathbf{W} + \omega_r\mathbf{L}_{\alpha\beta}\mathbf{J}\right)\boldsymbol{i}^{\star}_s(k+1) + \boldsymbol{v}_{ind}(k)\right] \tag{21}$$

where $\mathbf{J}$ is the 90 rotation matrix. The open-loop or steady-state control input $\boldsymbol{u}_{ss}(k)$ is determined from (3) and ensures that the output currents follow their references under ideal conditions in which both, the disturbances and the system parameters, are known with certainty.

Therefore, by inspecting (19), it is shown that $\boldsymbol{\Lambda}_u$ allows to modify the dynamic response and robustness properties of the closed-loop system. More details on the methodology used to design the parameters of the tuning matrix $\boldsymbol{\Lambda}_u$ will be presented in Section III-C. As described in (19), for each region $\mathcal{R}_j \in \mathcal{R}$, the cost function is expressed as a function of the matrix $\boldsymbol{U}_j$ and the normalized application times $\boldsymbol{d}_j$. Consequently, the OSS is obtained by solving, at each control period k, the following OSS-MPC problem:

$$\{\boldsymbol{U}^{\star}, \boldsymbol{d}^{\star}\} = \arg\min_{\boldsymbol{U}_j}\left\{\min_{\boldsymbol{d}_j} J_j\left(\boldsymbol{d}_j, \boldsymbol{U}_j\right)\right\} \tag{22a}$$

$$\text{s.t. } \mathbb{1}^{\top}\boldsymbol{d}_j = 1 \tag{22b}$$

$$\boldsymbol{d}_j \geq 0. \tag{22c}$$

Notice that the optimal control problem underlying the OSS-MPC (22) considers two nested optimizations. First, in the internal optimization step, a local minimum solution $\boldsymbol{d}_j$ is obtained for the jth SS candidate ($\mathcal{R}_j \in \mathcal{R}$). Then, in the external optimization stage, the pair $\{\boldsymbol{U}^{\star}, \boldsymbol{d}^{\star}\}$ that provides the minimum value of the cost function defines the global optimal SS for machine control. This strategy implies that six constrained optimal problems must be solved and then deciding between the smallest of them.

However, this work proposes a more efficient method to solve the problem by calculating the unconstrained solution of the internal optimization step. This approach significantly reduces the complexity, allowing one to reduce the global problem of six multivariable optimization problems into a global problem of one multivariable optimization in the nonovermodulated case and three single-variable optimization problems in the overmodulated case, each one with an explicit analytical solution. To do that, the nonnegative constraint in (22c) is ignored to compute the unconstrained solution first.

Using the method of Lagrange multipliers [16], the unbounded solution of (22) for each candidate SS j is given by [17]

$$\boldsymbol{d}_{rj} = \begin{bmatrix}\boldsymbol{U}_j \\ \mathbb{1}^{\top}\end{bmatrix}^{-1}\begin{bmatrix}\boldsymbol{u}_{uc}(k) \\ 1\end{bmatrix} \tag{23}$$

where $\boldsymbol{u}_{uc}(k)$ is the unconstrained ASV defined as follows:

$$\boldsymbol{u}_{uc} = \left(\mathbf{B}^{\top}\mathbf{B} + \boldsymbol{\Lambda}^{\top}_u\boldsymbol{\Lambda}_u\right)^{-1}\left(\mathbf{B}^{\top}\mathbf{B}\boldsymbol{u}_{db} + \boldsymbol{\Lambda}^{\top}_u\boldsymbol{\Lambda}_u\boldsymbol{u}_{ss}\right). \tag{24}$$

By rewriting the cost function (19) in terms of $\boldsymbol{u}_{uc}$, we have

$$J(\boldsymbol{u}) = \left(\boldsymbol{u} - \boldsymbol{u}_{uc}\right)^{\top}\left(\mathbf{B}^{\top}\mathbf{B} + \boldsymbol{\Lambda}^{\top}_u\boldsymbol{\Lambda}_u\right)\left(\boldsymbol{u} - \boldsymbol{u}_{uc}\right) + c \tag{25}$$

where $c = c(k)$ does not depend on the decision variable $\boldsymbol{u}$. In contrast to the controller introduced in [17] and [18], the level sets of the cost function (25) describe ellipses centered at $\boldsymbol{u}_{uc}(k)$, as shown in Fig. 5(a), which difficulties the process of obtaining the optimal solution. In this regard, the optimal average switching vector (OASV) for the original problem (22) $\boldsymbol{u}^{\star}$ corresponds to the point in the $\alpha\beta$ plane where the first level set around $\boldsymbol{u}_{uc}$ have a common point with the feasible region $\mathbb{F}$ [i.e., hexagon shown in Fig. 5(a)]. Any solution $\boldsymbol{u}_{uc}$ is associated to a convex cone formed by the active vectors of a given region

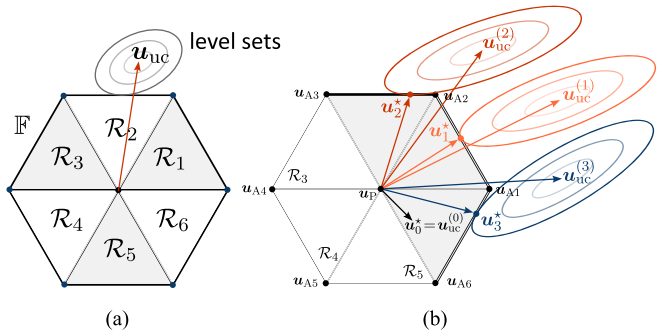

Fig. 5. Overmodulation and unbounded solutions. (a) Level sets in the $\alpha\beta$ plane. (b) Relation to the optimal solution $\boldsymbol{u}^\star$.

$\mathcal{R}_{j_{\rm uc}}$. Such a region with subscript $j_{\rm uc}$ is found as follows:

$$j_{\rm uc} = \text{floor}\left\{\frac{6}{\pi}\tan^{-1}\left(\frac{u_{{\rm uc}\beta}}{u_{{\rm uc}\alpha}}\right)\right\}+1. \tag{26}$$

In case $\boldsymbol{u}_{\rm uc}(k)\in\mathbb{F}$, then it corresponds to the optimal value of the original problem (22) and $\boldsymbol{u}_{\rm s}^\star(k)=\boldsymbol{u}_{\rm uc}$ [e.g., $\boldsymbol{u}_{\rm uc}^{(0)}$ in Fig. 5(b)]. In this case $\mathcal{R}_{j_{\rm opt}}=\mathcal{R}_{j_{\rm uc}}$ and $\boldsymbol{d}^\star=\boldsymbol{d}_{{\rm r}j}$.

Nevertheless, the controller may provide unfeasible solutions under some operating conditions. Specifically, the vector $\boldsymbol{u}_{\rm uc}(k)$ could fall outside the control region during transients and $\boldsymbol{u}_{\rm uc}(k)\notin\mathbb{F}$. This condition can be detected when the unbounded solution (23) provides a negative duty cycle for the passive vectors ($d_{\rm rp}<0$) to compensate for the overapplication of the active switching vectors. Thus, the optimal solution necessarily lies on the parameter of the feasible region. However, unlike in [17], it cannot be assumed that $\mathcal{R}_{j_{\rm opt}}$=$\mathcal{R}_{j_{\rm uc}}$ in this scenario. This is illustrated by the three examples depicted in Fig. 5(b). Among these, only example $\boldsymbol{u}_{\rm uc}^{(1)}$ shows the unconstrained solution projected onto the optimal region. In contrast, the unconstrained solutions $\boldsymbol{u}_{\rm uc}^{(2)}$ and $\boldsymbol{u}_{\rm uc}^{(3)}$ do not define the optimal region due to the properties of the ellipsoids. To address this issue and obtain the optimal solution during overmodulation without computing the eigenvalues of matrix $\mathbf{B}^\top\mathbf{B}+\mathbf{\Lambda}_u^\top\mathbf{\Lambda}_u$, it is proposed to search within the region associated with $\mathcal{R}_{j_{\rm uc}}$ and its two neighboring regions. This approach limits the optimization process to only three candidate regions. Consequently, for each candidate region $j\in\{j_{\rm uc}-1, j_{\rm uc}, j_{\rm uc}+1\}$, the following optimization problem must be solved:

$$\{\boldsymbol{U}^\star,\boldsymbol{d}^\star\} = \arg\min_{\boldsymbol{U}_j}\left\{\min_{\boldsymbol{d}_j} J_j\left(\boldsymbol{d}_j,\boldsymbol{U}_j\right)\right\} \tag{27a}$$

$$\text{s.t }.\mathbb{1}^\top\boldsymbol{d}_j = 1 \tag{27b}$$

$$\boldsymbol{z}^\top\boldsymbol{d}_j = 0 \tag{27c}$$

$$\boldsymbol{d}_j \geq 0. \tag{27d}$$

The constant $\boldsymbol{z}=[100]^\top$ in the constraint (27c) implies that the solution lies on the parameter of the region $\mathbb{F}$. The solution of (27) can be found by substituting $\boldsymbol{d}_j=d_{1j}\boldsymbol{x}+\boldsymbol{y}$ in the objective function, with $\boldsymbol{x}=[01-1]^\top$ and $\boldsymbol{y}=[001]^\top$. The unbounded solution of (27) is given by

$$d_{1j}^{\rm ub} = \frac{\boldsymbol{x}^\top\boldsymbol{U}_j^\top\left[\mathbf{B}^\top\mathbf{B}\left(\boldsymbol{u}_{\rm db}-\boldsymbol{U}_j\boldsymbol{y}\right)+\mathbf{\Lambda}_u^\top\mathbf{\Lambda}_u\left(\boldsymbol{u}_{\rm ss}-\boldsymbol{U}_j\boldsymbol{y}\right)\right]}{\boldsymbol{x}^\top\boldsymbol{U}_j^\top\left[\mathbf{B}^\top\mathbf{B}+\mathbf{\Lambda}_u^\top\mathbf{\Lambda}_u\right]\boldsymbol{U}_j\boldsymbol{x}} \tag{28}$$

and the optimal solution is computed from it as

$$\begin{aligned} d_{{\rm p}j}^\star &= 0\\ d_{1j}^\star &= \text{mid}\left\{0, d_{1j}^{\rm ub}, 1\right\}\\ d_{2j}^\star &= 1-d_{1j}^\star \end{aligned} \tag{29}$$

where $\text{mid}\{\cdot\}$ defines the median of the components. Finally, the candidate solution that delivers the lowest objective value J_j in (27a) corresponds to the global optimal solution to be applied by the converter.

C. Tuning of the Controller

The design of the tuning matrix $\mathbf{\Lambda}_u$ is straightforward. As shown in (24), $\boldsymbol{u}_{\rm uc}$ is the weighted sum between the deadbeat and the steady-state control inputs. It follows that by choosing $\mathbf{\Lambda}_u=\mathbf{B}$, the resulting control action will give equal priority to the stator current tracking error and the control effort. Thus, using a tuning matrix $\mathbf{\Lambda}_u$ large compared to $\mathbf{B}$, the converter will apply a mean switching vector close to $\boldsymbol{u}_{\rm ss}(k)$, leading to open-loop operation. On the contrary, if $\mathbf{\Lambda}_u\approx 0$, the first term of the cost function (19) becomes predominant and, therefore, the converter tends to synthesize the deadbeat control action $\boldsymbol{u}_{\rm db}(k)$ in (20), which increases the bandwidth of the controller [19].

To regulate this phenomenon, it is convenient to incorporate the tuning factors $\lambda_{u\alpha}$ and $\lambda_{u\beta}$ according to

$$\mathbf{\Lambda}_u(k) = \text{diag}\left(\lambda_{u\alpha},\lambda_{u\beta}\right)\mathbf{B}(k). \tag{30}$$

Thus, the tuning parameters can be adjusted to increase ($\lambda_{ux}<1$) or decrease ($\lambda_{ux}>1$) the closed-loop dynamics.

D. DC Current Control

The dc current control stage is proposed to control $i_{\rm dc2}$ using the degree of freedom (redundancy) of the passive vector, by distributing it in an optimal way by means of the distribution factor ϑ, as presented in (12). In that sense, the optimization problem is posed by

$$\vartheta^\star = \min_{\vartheta}\left(i_{\rm dc2}(k+1)(\vartheta)-i_{\rm dc2}^\star\right)^2 \tag{31a}$$

$$\text{s.t }.\vartheta\in[0,1]. \tag{31b}$$

Replacing (15) in (31a) solves the 1-D problem for the parameter $\vartheta^\star$, whose relaxed solution is

$$\vartheta_{\rm unc} = \frac{L_{\rm dc2}}{3V_{\rm dc1}d_{\rm p}^\star T_{\rm h}}\left[i_{\rm dc2}(k)-i_{\rm dc2}^\star+\frac{3T_{\rm h}}{L_{\rm dc2}}\left\{V_{\rm dc2}\frac{1}{1}\right.\right.$$
$$\left.\left.-\frac{R_{\rm dc2}i_{\rm dc2}}{3}-V_{\rm dc1}\left(d_1^\star u_{0(1)}^\star+d_2^\star u_{0(2)}^\star\right)\right\}\right]. \tag{32}$$

Because (31a) is a constrained one-variable quadratic problem, the optimal solution is found by saturating the relaxed solution

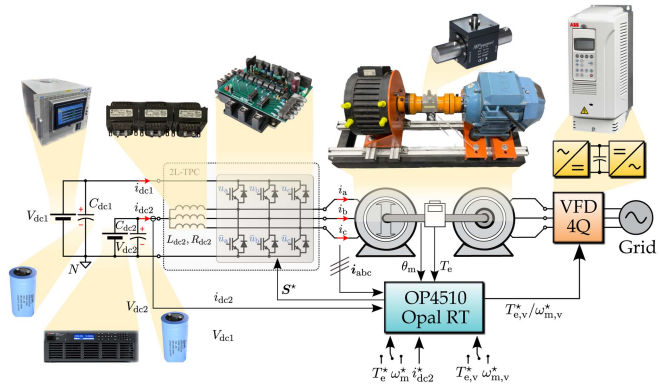

Fig. 6. Experimental setup.

(32) in the bounds (31b), so the solution is

$$\vartheta^\star = \text{mid}\left\{0, \vartheta_{\text{unc}}, 1\right\}. \tag{33}$$

Finally, the values of $d_0^\star$ and $d_3^\star$ are retrieved by (12) and thus the OSS $\boldsymbol{S}^\star$ to apply in the converter is determined. For this reason, when the machine control selects an OASV with large modulation index, i.e., when $d_{\text{p}}^\star$ is small, the influence of the value of $\vartheta^\star$ is smaller and therefore the control of i_{dc2} becomes more limited.

The specific values of $i_{\text{dc2}}^\star$ depend on the requirements of each particular application, and is managed by a high-level controller [20] However, several benchmarks at specific time intervals are addressed in Section IV to analyze power transfers across different ports.

IV. Experimental Results

This section evaluates the performance of the proposed control strategy. For this purpose, the control algorithm was implemented in an Opal-RT OP4510 controller whose main processing unit is complemented with very high speed (200 MHz) Xilinx KINTEX-7 FPGA technology. The system is integrated with 16-bit analog-to-digital converters and the modulator is carrier-based to synthesize the desired OSS. The control algorithm was also experimentally validated with a low-cost Texas Instruments TMS320F28379D controller in the early testing phase. The experimental tests use two bidirectional dc power sources and an anisotropic PMSM coupled to an induction machine to evaluate the control system during stationary, transient and different operating conditions, as illustrated in Fig. 6. The system parameters are summarized in Table I. A ratio between the dc voltages of 2:1 has been used since this operation ensures maximum power extraction from the 2L-TPC converter. However, when this ratio is disturbed, the power extraction is limited [20].

A. Steady-State Speed Performance

To evaluate the system performance, the total harmonic distortion (THD) and weighted total harmonic distortion (WTHD) are calculated for the voltages and currents. The steady-state behavior of the stator currents in the $\alpha\beta$ frame is shown in Fig. 7. The shaft speed has been set to $\omega_{\text{m}} = 1500$ r.p.m. and current references $\|\boldsymbol{i}_{\text{s}}^\star\| = \{20, 40\}$ A have been imposed. In this configuration, the average modulation index for each case determined as the ratio of the modulus of the voltage to its maximum possible steady-state value [21] is $\bar{m} = \{0.57, 0.61\}$, respectively. It is also clear how the phase-neutral voltage of the converter v_{aN} oscillates between two levels, while the phase-to-phase voltage v_{ab} oscillates between three levels.

TABLE I
Base Parameters and Conditions of the Experimental Setup

Category	Description	Symbol	Value
2L-TPC	dc1 port voltage	V_{dc1}	50 V
	dc2 port voltage	V_{dc2}	25 V
	dc2 converter inductance	L_{dc2}	5.31 mH
	dc2 converter resistance	R_{dc2}	110.3 mΩ
PMSM	d-axis inductance	L_{d}	45.71 μH
	q-axis inductance	L_{q}	71.11 μH
	Resistance	R_{s}	4.9 mΩ
	Flux	ψ_{m}	17.66 mWb
	Pole pairs	p	4
	Nominal current	I_{nom}	127.5 A
	Nominal speed	ω_{nom}	6000 r.p.m.
	Nominal power	P_{nom}	11.0 kW
Control	Switching frequency	$f_{\text{s}} = f_{\text{s}}^{\text{oss}}$	20 kHz
	Switching period	$T_{\text{s}} = T_{\text{s}}^{\text{oss}}$	$1/f_{\text{s}}$ s
	α-axis tunning parameter	$\lambda_{u\alpha}$	1.0 pu
	β-axis tunning parameter	$\lambda_{u\beta}$	1.0 pu

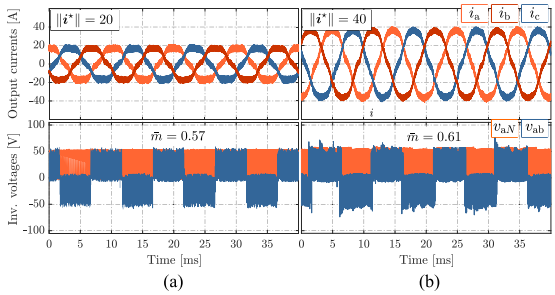

Fig. 7. Steady-state performance at $\omega_{\text{m}} = 1500$ r.p.m. and $f_{\text{s}} = 20$ kHz for two different current references $\|\boldsymbol{i}_{\text{s}}^\star\|$. (a) 20 A ($\bar{m} = 0.57$). (b) 40 A ($\bar{m} = 0.61$).

Fig. 8 shows the harmonic spectrum for the current, phase voltage in the phase a and phase-phase voltage for the operating conditions of Fig. 7. For the current, the dominant harmonics are the 5th and 11th in the case of a low current level. As the reference is doubled, the 5th harmonic decreases and a 7th harmonic appears. Regarding the phase voltages, it contains harmonics centered at the switching frequency $f_{\text{s}} = 20$ kHz and multiples of it. In addition, a high value in the 3rd harmonic for the voltage v_{aN} is observed, as a consequence of a modulation with space vector modulation (SVM) strategy (in an implicit manner) [22]. However, that third harmonic disappears in the line-to-line voltage spectrum and in the current spectrum. THD decreases as the reference increases for all signals, while WTHD decreases significantly for higher current reference.

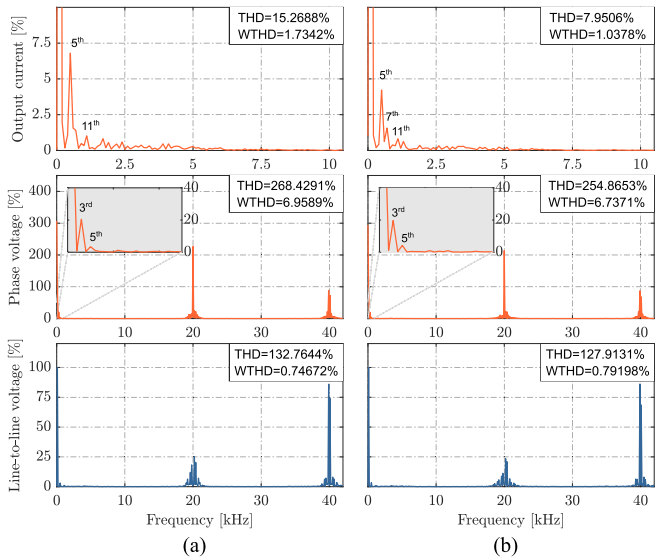

Fig. 8. Harmonic spectrum for i_{a}, $v_{\mathrm{a}N}$ and v_{ab} for two different current references $\|\boldsymbol{i}_{\mathrm{s}}^{\star}\|$. (a) 20 A. (b) 40 A.

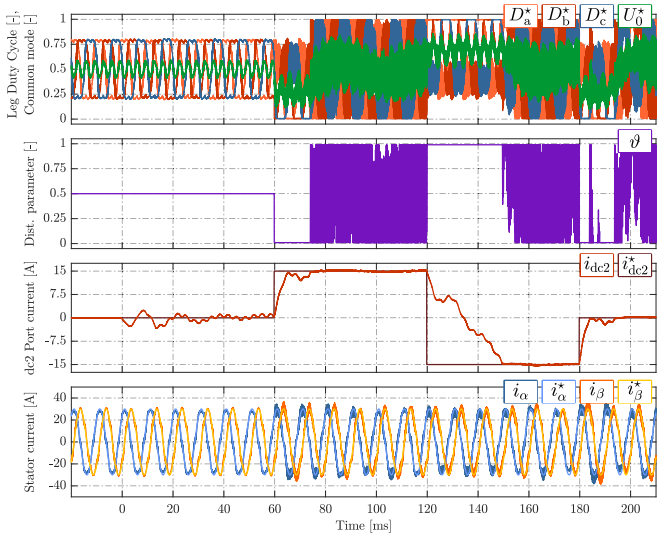

Fig. 9. Duty cycle waveforms per phase, common mode value, distribution parameter, and port DC2 and machine currents for: $\vartheta = 0.5 \rightarrow \vartheta^{\star}$.

B. Dc Port Current Control Performance

Fig. 9 illustrates a worst-case scenario test to evaluate the control of i_{dc2} by manipulating the common-mode voltage through the distribution parameter ϑ. The worst-case scenario occurs when the voltage vector operates at the maximum modulation index and at certain angles, where the CMV has no redundancy. To assess the effect of the distribution parameter ϑ, it was first set to an intermediate value of $\vartheta = 0.5$, and then adjusted to the optimal value $\vartheta^{\star}$. The induction machine was kept rotating at nominal speed all times.

At $t = 0$ ms, the port dc2 is electrically connected, but ϑ is intentionally fixed at $\vartheta = 0.5$ until $t = 60$ ms. During this time, i_{dc2} remains uncontrolled but reaches a stable equilibrium near

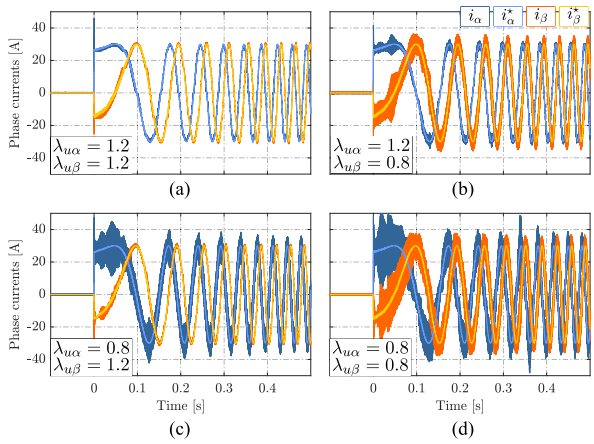

Fig. 10. Effect of the tuning parameters $\lambda_{u\alpha}, \lambda_{u\beta}$ on the transient performance of the controller for $i_{\mathrm{q}}^{\star}$: $0 \rightarrow 30$ A. (a) $\lambda_{u\alpha}$, $\lambda_{u\beta}$: 1.2, 1.2. (b) $\lambda_{u\alpha}$, $\lambda_{u\beta}$: 1.2, 0.8. (c) $\lambda_{u\alpha}$, $\lambda_{u\beta}$: 0.8, 1.2. (d) $\lambda_{u\alpha}$, $\lambda_{u\beta}$: 0.8, 0.8.

$i_{\mathrm{dc2}} = 0$ A. The modulation signals exhibit characteristics typical of SVM strategies with uniformly distributed passive vectors, and the common-mode trajectory of the ASV (13) follows a triangular path, as described in [23].

From $t = 60$ ms onward, $\vartheta^{\star}$ is dynamically adjusted by the dc port current control to track the reference $i_{\mathrm{dc2}}^{\star}$. When i_{dc2} increases, the control sets $\vartheta^{\star} = 0$, and when it decreases, $\vartheta^{\star} = 1$. In addition, during the i_{dc2} transients, a perturbation with three times the fundamental frequency of the machine appears, caused by the common-mode oscillations imposed by the SVM and maintained by the machine current control in steady-state.

C. Effect of the Tuning Parameters

In this section, four experiments were carried out to demonstrate the effect of the tuning matrix $\boldsymbol{\Lambda}_u(k) = \mathrm{diag}(\lambda_{u\alpha}, \lambda_{u\beta})\mathbf{B}(k)$ on the dynamic behavior of the machine current control. For all the studied cases illustrated in Fig. 10, the machine starts stopped and a current step $i_{\mathrm{q}}^{\star}$: $0 \rightarrow 30$ A. Fig. 10(a) shows how a high value in both components of the matrix $\boldsymbol{\Lambda}_u(k)$ produces a smooth response in the reference tracking, although it may imply a higher overshoot in the current reference change due to a smooth transition in the voltage change. Fig. 10(b) shows how a low value in the β component induces much more aggressive tracking by a dominance in the deadbeat control input, causing measurement errors in a real experiment to result in much more oscillating and noisy responses around the reference of that component. Similarly, Fig. 10(c) shows that the α component has a well-aggressive tracking. Finally Fig. 10(d) shows a generalized aggressive response where the deadbeat control dominates globally in both components. It can be seen how both $\alpha\beta$ coordinates can be tuned practically uncoupled and independently of each other.

D. Variable-Speed Control Performance

The experiments of Fig. 11 test the speed controller. At $t = 0$ s a reference change in speed occurs to bring the machine to nominal speed. At that time the controller saturates the quadrature

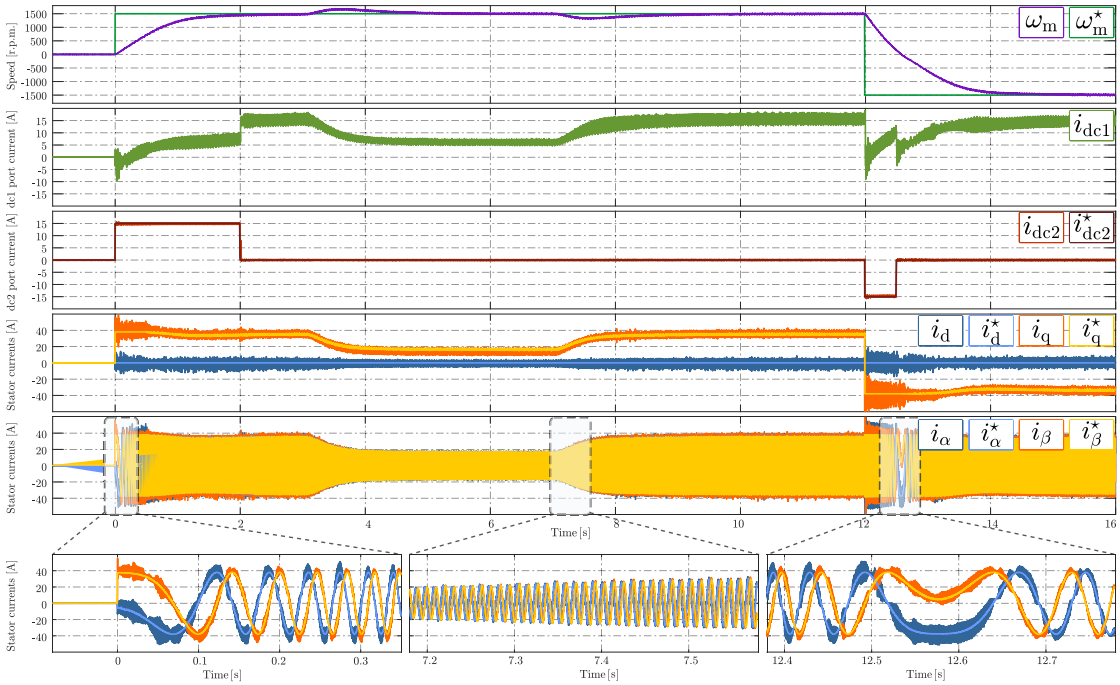

Fig. 11. Operation of the 2L-TPC with speed control and mechanical disturbance in the load torque.

current at its maximum. In addition, a reference change occurs at $i_{dc2}^\star$ so that the dc2 port contributes power. At $t = 2$ s the dc2 port stops contributing its energy and consequently, the dc1 port increases the value of its current to compensate it. At $t = 3.1$ s the mechanical load is perturbed with a reduction in load torque. As a consequence the speed controller adjusts to the reference and decreases the value of $i_q^\star$ along with the current provided by the dc1 port. At $t = 7.1$ s the torque reduction is eliminated and the original load conditions are acquired again. At $t = 12$ s a reference change in speed occurs to bring the machine to nominal speed in the opposite direction. At $t = 12$ s there is a reference change in speed to a nominal value but in the negative direction. At that time the controller saturates the quadrature current at its minimum and operates in regenerative mode. In addition, the reference $i_{dc2}^\star$ is changed to a negative value so that the dc2 port injects the regenerated energy. At $t = 12.58$ s the machine reaches speed $\omega_m^\star \approx 0$ r.p.m. and undergoes a change of rotation. At that moment the dc2 port stops receiving energy and consequently all the energy needed to run the machine as a motor (but in the opposite direction) comes from the dc1 port. Finally the machine reaches its equilibrium speed and keeps rotating at its nominal speed but with negative sign. It should be noted that in conditions where $i_{dc2}^\star$ and $i_q^\star \backsim T_e$ are constant, the profile of i_{dc1} is similar to that of mechanical speed ω_m because V_{dc1} is constant and the mechanical power corresponds to the product between ω_m and T_e.

E. Dynamics of Energy Transfer Between Ports

Three tests were performed to demonstrate the power transfer between two ports of the converter while keeping the third port stable with the machine rotating at nominal speed. In process I [see Fig. 12(a)], a transition is performed at ac port according to $i_q^\star = 30 \rightarrow -30$ A for 0.1 s while keeping fixed the value of $i_{dc2}^\star = 10$ A. It is observed how the value of i_{dc1} also varies in the form of a ramp, similar to i_q. In process II [see Fig. 12(b)], the same transition is performed at the ac port as in process I but the value of $i_{dc2}^\star$ which cancels the current i_{dc1} is determined theoretically with a power balance as follows:

$$i_{dc2}^\star(k) = \frac{\omega_m T_e^\star(k)}{V_{dc2}}. \tag{34}$$

Consequently, the value of $i_{dc1} \approx 0$ A under ideal conditions and the difference is explained by system inefficiencies. It is observed how i_{dc2} varies in the form of a ramp similar to i_q. Finally, in process III [see Fig. 12(c)] the machine is kept operating at current stationary conditions. A ramp transition is made for the reference $i_{dc2}^\star = 10 \rightarrow -10$ A. Consequently, i_{dc1} also varies in the form of a ramp but in the opposite way, since all the power that is no longer injected from dc2 port must be supplied by dc1. The variation of current i_{dc2} is $\Delta i_{dc2} = -20$ A and that of i_{dc1} is exactly half $\Delta i_{dc1} = 10$ A due to the voltage ratio between dc ports.

F. Simulated OSV-MPC Implementation as Benchmark

To evaluate the performance of the OSS-MPC it is necessary to compare it with the traditional control method OSV-MPC. This strategy applies one of the 2^3 possible switching vectors $\boldsymbol{u}_{abc} \in \mathbb{U} \triangleq \{0, 1\}^3$ minimizing the cost function

$$J_j = \left\| \mathbf{B} \left(\boldsymbol{U}_j \boldsymbol{d}_j(k) - \boldsymbol{u}_{db}(k) \right) \right\|_2^2 + \left\| \boldsymbol{\Lambda}_u \left(\boldsymbol{U}_j \boldsymbol{d}_j(k) - \boldsymbol{u}_{ss}(k) \right) \right\|_2^2$$

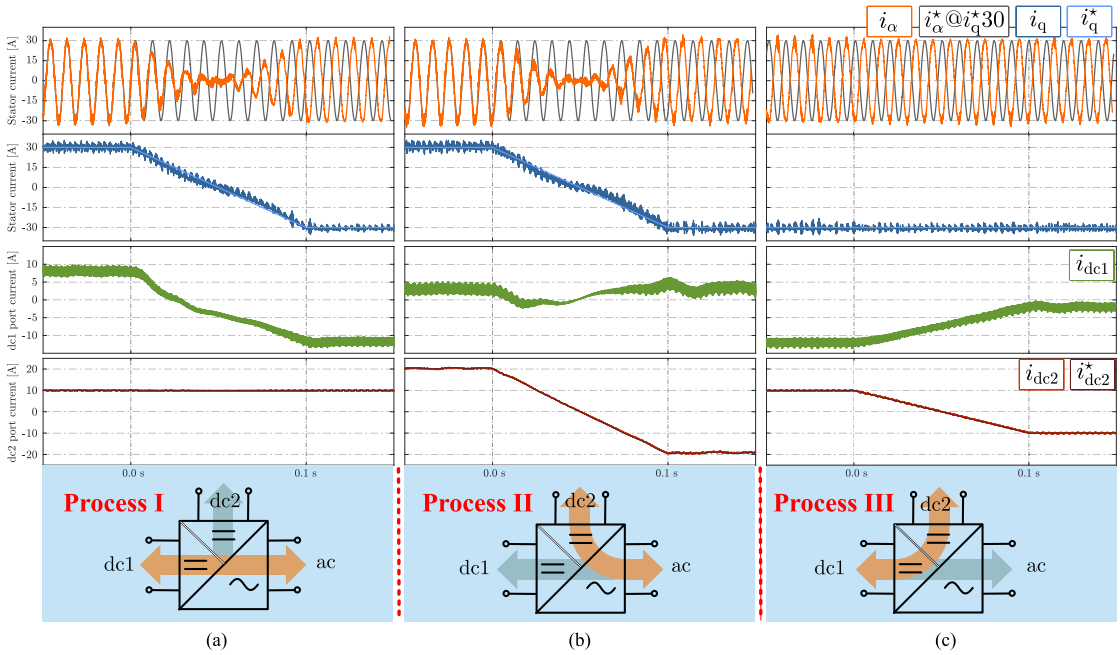

Fig. 12. Dynamics in energy transfer between ports for: (a) process I, (b) process II, and (c) process III.

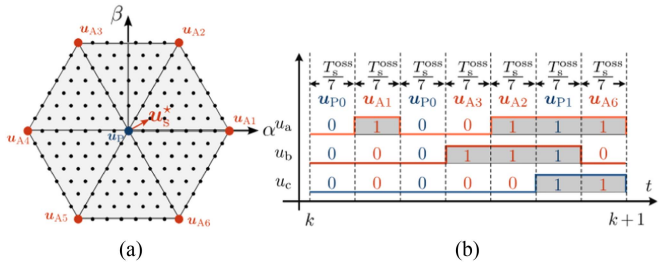

Fig. 13. Selection of switching vectors for OSV-MPC current control. (a) Vector space during $T_s^{oss} = 7T_s^{osv}$. (b) Switching pattern.

$$+ \lambda_{dc2} \left\| i_{dc2}(k) - i_{dc2}^\star(k+1) \right\|_2^2 \tag{35}$$

which is analogous to (19), but a third member has been added that penalizes the tracking error of i_{dc2} by the λ_{dc2} parameter.

As OSS-MPC applies seven switching states within a period $T_s = T_s^{oss}$ and OSV-MPC applies one switching state in its control period T_s^{osv}, a fair comparison with a similar number of commutations requires that $T_s^{osv} = T_s^{oss}/7$. The feasible region of an ASV with OSV during a period T_s corresponds to all combinations of an average of seven of the eight possible switching vectors, as shown in Fig. 13(a). For example, applying the switching pattern in Fig. 13(b), the resulting ASV is $\boldsymbol{u}_s^\star$.

The simulation computation time during a period T_s has been calculated for both methods using MATLAB tic and toc functions. For the OSS-MPC strategy, this corresponds to 296μs, while for the OSV-MPC strategy it increases to 644 μs.

Fig. 14 shows the current waveforms in steady state with the harmonic spectrum for both control methods. Fig. 14(a) shows that the OSV strategy exhibits current tracking with a larger

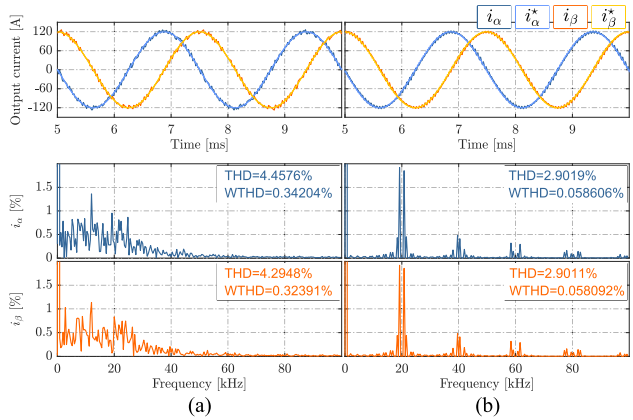

Fig. 14. Steady-state performance. (a) OSV-MPC strategy with $f_s^{osv} = 7f_s^{oss}$ kHz. (b) OSS-MPC strategy with $f_s^{oss} = 20$ kHz.

ripple. The harmonic spectrum is dispersed with considerable low-frequency components. Fig. 14(b) shows that OSS has a tracking with even ripples and its harmonic spectrum is sharp, with values around multiples of the switching frequency f_s^{oss} corresponding to high frequencies, which facilitates filtering. The THD decreases by about 35% while the WTHD decreases by 85% because it penalizes the high-frequency components present in OSV-MPC.

Fig. 15 shows four different cases for the dynamic response under step changes in ac and dc2 port currents. With the OSS strategy [see Fig. 15(a)], during the stator current transition, the value of i_{dc2} tends to 0 for a brief instant because the value of $u_{s\beta}^\star$ is at the parameter of the feasible region, so $d_p = 0$ and consequently the dc port current control has no control over the system at that instant. In OSV strategy [see Fig. 15(b), (c),

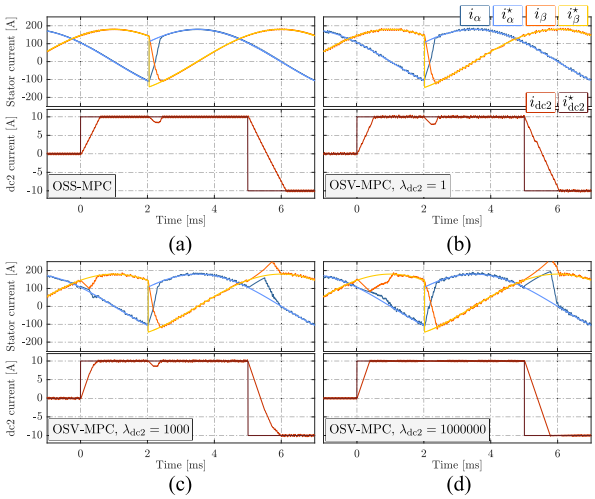

Fig. 15. Dynamic currents responses $\|\boldsymbol{i}_s^\star\| = 127.5\sqrt{2}$ A and $\|i_{dc2}\| = 15$ A. (a) OSS-MPC. (b) OSV-MPC, $\lambda_{dc2} = 1$. (c) OSV-MPC, $\lambda_{dc2} = 1000$ y. (d) OSV-MPC, $\lambda_{dc2} = 1\,000\,000$.

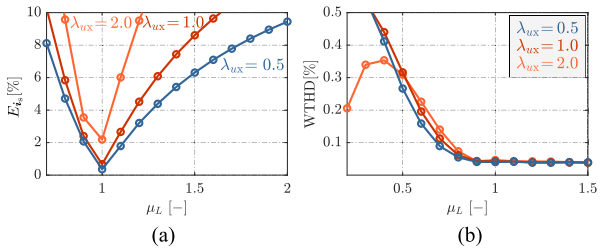

Fig. 16. Effect of the parameter μ_L for different values of λ_{ux} on: (a) average current tracking error $E_{\boldsymbol{i}_s}$ % and (b) WTHD, at nominal operating point.

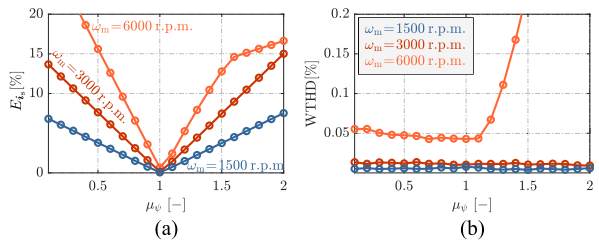

Fig. 17. Effect of the parameter μ_ψ for different values of ω_m on: (a) average current tracking error $E_{\boldsymbol{i}_s}$ % and (b) WTHD, at nominal operating point.

and (d)] the parameter λ_{dc2} affects current tracking and there is a trade off between stator or dc2. It can be further observed that the OSV-MPC strategy has a slight superiority in dynamic response over OSS-MPC, even for different values of λ_{dc2}.

G. Sensitivity Analysis

The machine parameter mismatches are modeled as $\hat{L}_d = \mu_L L_d$, $\hat{L}_q = \mu_L L_q$, $\hat{R}_s = \mu_R R_s$, and $\hat{\psi}_m = \mu_\psi \psi_m$. Fig. 16 shows the impact on the machine operating in steady state considering a wide variation of the parameter μ_L. The average current tracking error is reduced for low values of λ_{ux} and the WTHD has a stable behavior in the case of overestimation. Fig. 17 shows an analogous test, but considering a variation in the parameter μ_ψ for different rotor speeds ω_m. In this case, the average current tracking error is reduced for low values of speed and grows linearly with respect to the deviation of the μ_ψ factor and the WTHD has a stable behavior in the case of underestimation.

V. Conclusion

This article proposes an MPC strategy based on OSS for 2L-TPC converters driving an anisotropic PMSM with hybrid energy storage. Extensive experimental tests demonstrate that the proposed control method performs optimally under both stationary and transient conditions. The OSS-MPC controller ensures the converter operates with a fixed switching frequency and a predefined harmonic spectrum without compromising the fast dynamic response characteristic of predictive control strategies. In addition, the redundancy of passive vectors can be utilized to manipulate the common-mode switching signal to control the current of the dc ports. Consequently, the proposed controller is suitable for 2L-TPC applications that drive machines with energy storage, requiring high dynamic response and the simultaneous handling of all converter currents in the same stage.

References

[1] F. Rubio and J. Pereda, "Optimal switching sequence model predictive control for a three-port converter," in *Proc. 2023 IEEE Energy Convers. Congr. Expo.*, 2023, pp. 3669–3676.

[2] G. Wang, T. Li, G. Zhang, X. Gui, and D. Xu, "Position estimation error reduction using recursive-least-square adaptive filter for model-based sensorless interior permanent-magnet synchronous motor drives," *IEEE Trans. Ind. Electron.*, vol. 61, no. 9, pp. 5115–5125, Sep. 2014.

[3] S. Neira, Z. Blatsi, M. M. Merlin, and J. Pereda, "A technical overview of single-stage three-port DC-DC-AC converters," in *Proc. 24th Eur. Conf. Power Electron. Appl.*, 2022, pp. 01–11.

[4] S. Neira, J. Pereda, and F. Rojas, "Three-port full-bridge bidirectional converter for hybrid DC/DC/AC systems," *IEEE Trans. Power Electron.*, vol. 35, no. 12, pp. 13077–13084, Dec. 2020.

[5] T. Geyer, *Model Predictive Control of High Power Converters and Industrial Drives*. Hoboken, NJ, USA: Wiley, 2016.

[6] S. Vazquez, J. Rodriguez, M. Rivera, L. G. Franquelo, and M. Norambuena, "Model predictive control for power converters and drives: Advances and trends," *IEEE Trans. Ind. Electron.*, vol. 64, no. 2, pp. 935–947, Feb. 2017.

[7] D. E. Quevedo, R. P. Aguilera, and T. Geyer, *Predictive Control in Power Electronics and Drives: Basic Concepts, Theory, and Methods*. Berlin, Germany: Springer, 2014, pp. 181–226, doi: 10.1007/978-3-319-03401-0_5.

[8] P. Karamanakos, E. Liegmann, T. Geyer, and R. Kennel, "Model predictive control of power electronic systems: Methods, results, and challenges," *IEEE Open J. Ind. Appl.*, vol. 1, pp. 95–114, 2020.

[9] J. Rodriguez et al., "State of the art of finite control set model predictive control in power electronics," *IEEE Trans. Ind. Informat.*, vol. 9, no. 2, pp. 1003–1016, May 2013.

[10] S. Neira, J. Pereda, M. Merlin, and F. Rojas, "Three-port full-bridge cell for multilevel converters with battery energy storage," in *Proc. 2019 IEEE Energy Convers. Congr. Expo.*, 2019, pp. 6382–6387.

[11] J. Rodriguez et al., "Latest advances of model predictive control in electrical drives—Part I: Basic concepts and advanced strategies," *IEEE Trans. Power Electron.*, vol. 37, no. 4, pp. 3927–3942, Apr. 2022.

[12] T. Geyer, "A comparison of control and modulation schemes for medium-voltage drives: Emerging predictive control concepts versus PWM-based schemes," *IEEE Trans. Ind. Appl.*, vol. 47, no. 3, pp. 1380–1389, May/Jun. 2011.

[13] *The Instantaneous Power Theory*. Hoboken, NJ, USA: John Wiley and Sons, Inc., Ltd, ch. 3, pp. 37–109, 2017. [Online]. Available: https://onlinelibrary.wiley.com/doi/abs/10.1002/9781119307181.ch3

[14] M. Preindl and S. Bolognani, "Model predictive direct torque control with finite control set for PMSM drive systems, Part 1: Maximum torque per ampere operation," *IEEE Trans. Ind. Informat.*, vol. 9, no. 4, pp. 1912–1921, Nov. 2013.
[15] A. Mora, Ã. Orellana, J. Juliet, and R. Cãrdenas, "Model predictive torque control for torque ripple compensation in variable-speed PMSMs," *IEEE Trans. Ind. Electron.*, vol. 63, no. 7, pp. 4584–4592, Jul. 2016.
[16] S. Boyd and L. Vandenberghe, *Convex Optimization*. Cambridge, U.K.: Cambridge Univ. Press, 2004.
[17] A. Mora, R. Cárdenas-Dobson, R. P. Aguilera, A. Angulo, F. Donoso, and J. Rodriguez, "Computationally efficient cascaded optimal switching sequence MPC for grid-connected three-level NPC converters," *IEEE Trans. Power Electron.*, vol. 34, no. 12, pp. 12464–12475, Dec. 2019.
[18] A. Mora, R. Cardenas, R. P. Aguilera, A. Angulo, P. Lezana, and D. D.-C. Lu, "Predictive optimal switching sequence direct power control for grid-tied 3L-NPC converters," *IEEE Trans. Ind. Electron.*, vol. 68, no. 9, pp. 8561–8571, Sep. 2021.
[19] A. Mora et al., "Optimal switching sequence MPC for four-leg two-level grid-connected converters," *IEEE Trans. Emerg. Sel. Topics Power Electron.*, vol. 12, no. 2, pp. 1271–1281, Apr. 2024.
[20] A. Lizana, J. Pereda, F. Rubio, and F. Rojas, "Finite control set model predictive current control (FCS-MPCC) of three-port converter for fuel cell hybrid electric vehicles," *IEEE Trans. Veh. Technol.*, pp. 1–9, 2024, doi: 10.1109/TVT.2024.3476924.
[21] A. Mora, "Optimal switching sequence model predictive control for power electronics," Ph.D. dissertation, Universidad de Chile, Santiago, Chile, 2019. [Online]. Available: https://repositorio.uchile.cl/handle/2250/170522
[22] J. Holtz and N. Oikonomou, "Estimation of the fundamental current in low-switching-frequency high dynamic medium-voltage drives," *IEEE Trans. Ind. Appl.*, vol. 44, no. 5, pp. 1597–1605, Sep./Oct. 2008.
[23] J. Holtz, "Pulsewidth modulation for electronic power conversion," *Proc. IEEE*, vol. 82, no. 8, pp. 1194–1214, Aug. 1994.

Felipe Rubio received the B.Sc. (Hons.) and M.Sc. degrees in electrical engineering from Pontificia Universidad Católica de Chile, Santiago, Chile, in 2021 and 2024, respectively.

Since 2021, he has been part of the Power and Energy Conversion Laboratory, Pontificia Universidad Católica de Chile. His research interests include predictive control of power converters, control of multiport power converters applied to energy storage systems, control systems applied to electric vehicles, renewable energy, ac and dc electric networks, industrial applications, and variable speed drives.

Javier Pereda (Senior Member, IEEE) received the B.Sc. (Eng.) (Hons.) degree in 2009, and the M.Sc. and Ph.D. degrees, in 2013, from Pontificia Universidad Católica de Chile, Santiago, all in electrical engineering.

In 2013, he joined the Electrical Department, Pontificia Universidad Católica de Chile, where he is currently an Associate Professor. From 2014 to 2016, he was an Associate Research with the Control and Power Group, Department of Electrical and Electronic Engineering, Imperial College London, London, U.K. He is an Associate Research with UC Energy Research Center, Chile, and the Solar Energy Research Center, Chile. He is the Principal Investigator of the Electric Vehicle Laboratory and the Power and Energy Conversion Laboratory, Pontificia Universidad Católica de Chile. His research interests include power electronics and control applied to electric vehicles, energy storage, ac and dc electric networks, renewable energy, multilevel converters, industrial applications, and motor drives.

Andrés Mora (Member, IEEE) received the B.Sc. and M.Sc. (Hons.) degrees from the Universidad Técnica Federico Santa María (UTFSM), Valparaíso, Chile, in 2007 and 2010, respectively, and the Ph.D. degree from the Universidad de Chile, Santiago, Chile, in 2019, all in electrical engineering.

In 2011, he joined the Electrical Department, UTFSM, where he is currently an Associate Professor. Since 2023, he has been an Associate Researcher with the Advanced Center for Electrical and Electronic Engineering, Universidad Técnica Federico Santa María.

Dr. Mora was the recipient of the IEEE Transactions on Industrial Electronics Best Paper Award in 2019. His research interests include advanced control techniques applied to modular multilevel converters, variable speed drives, and microgrids.

Félix Rojas (Member, IEEE) received the B.Eng. and M.Sc. (Hons.) degrees from the Universidad de Santiago de Chile, Santiago, Chile, in 2009, and the Ph.D. degree from the Technical University of Munich, Munich, Germany, in 2016, all in electrical engineering.

From 2016 to 2021, he was an Associate Professor in electrical engineering with the University of Santiago, Santiago, Chile, and the Head of the Electrical Energy Technologies Research Center, USACH. He is currently an Associate Professor with Electrical Department, Pontificia Universidad Católica de Chile, Santiago, Chile, and the Principal Investigator of the Electric Vehicle Laboratory and the Power and Energy Conversion Laboratory (PEClab). He is also an Associate Research with the Solar Energy Research Center (SERC Chile) and the UC Energy Research Center.